Trace doping of multiple elements enables stable battery cycling of $LiCoO_2$ at 4.6 V

Jie-Nan Zhang[1,2†], Qinghao Li[1,3†], Chuying Ouyang[4], Xiqian Yu[1,2*], Mingyuan Ge[5], Xiaojing Huang[5], Enyuan Hu[5], Chao Ma[6], Shaofeng Li[7], Ruijuan Xiao[1], Wanli Yang[3], Yong Chu[5], Yijin Liu[7*], Huigen Yu[8], Xiao-Qing Yang[5], Xuejie Huang[1], Liquan Chen[1], Hong Li[1,2*]

1 Beijing Advanced Innovation Center for Materials Genome Engineering, Institute of Physics, Chinese Academy of Sciences, Beijing 100190, China.

2 Center of Materials Science and Optoelectronics Engineering, College of Materials Science and Opto-Electronic Technology, University of Chinese Academy of Sciences, Beijing 100049, China.

3 Advanced Light Source, Lawrence Berkeley National Laboratory, Berkeley, CA 94720, USA.

4 Department of Physics, Laboratory of Computational Materials Physics, Jiangxi Normal University, Jiangxi 330022, China.

5 Brookhaven National Laboratory, Upton, NY 11973, USA.

6 College of Materials Science and Engineering, Hunan University, Changsha 410082, China.

7 Stanford Synchrotron Radiation Lightsource, SLAC National Accelerator Laboratory, Menlo Park, CA 94025, USA.

8 Beijing WeLion New Energy Technology Co., Ltd., Beijing 102402, China.

Corresponding authors: X.Y. (xyu@iphy.ac.cn), Y.L. (liuyijin@slac.stanford.edu) and H.L. (hli@iphy.ac.cn)

$LiCoO_2$ is a dominant cathode material for Li-ion batteries due to its high volumetric energy density, which could potentially be further improved by charging to high voltage. Practical adoption of the high-voltage charging is, however, hindered by $LiCoO_2$'s structural instability at the deeply delithiated state and the associated safety concerns. Here, we achieve stable cycling of $LiCoO_2$ at 4.6 V (vs. Li/Li^+) through trace Ti-Mg-Al co-doping. By using state-of-the-art synchrotron X-ray imaging and spectroscopic techniques, we confirm the incorporation of Mg and Al into the $LiCoO_2$ lattice, which inhibits the undesired phase transition at voltages above 4.5 V. On the other hand, even in trace amount, Ti segregates significantly at grain boundaries and on the surface, modifying the microstructure of the particles while stabilizing the surface oxygen at high voltage. These dopants contribute though different mechanisms and synergistically promote the cycle stability of $LiCoO_2$ at 4.6 V.

The constantly increasing energy consumption of modern society has led to the demand for energy storage technology with higher energy densities[1,2,3]. Li-ion batteries (LIBs) are the most popular energy storage devices, which are widely deployed in portable electronics and, more recently, in electric vehicles. The energy density of LIBs is directly proportional to the working voltage and the lithium storage capacity. Therefore, the development of cathode materials that are of larger reversible capacity and are compatible with higher voltage charging has been a hot research topic[4,5,6,7]. Thanks to the tremendous research efforts devoted over the past few decades, we have witnessed the successful commercialization of quite a number of cathode materials (see the comparison of their theoretical energy densities in Supplementary Fig. 1). We note here that $LiCoO_2$, which was first recognised as a cathode material with good potential in the 1980s, still presents competitive or even superior energy density among all the cathode materials that are commercially available. As a key player on today's market of cathode materials, $LiCoO_2$ exhibits many essential advantages, including high theoretical capacity, high Li^+/electron conductivity, high theoretical density and high compressed density for electrode[8,9,10]. While the theoretical capacity of $LiCoO_2$ is as high as 274 mAh g^{-1}, its practical discharge capacity with acceptable level of cycle reversibility is only about 173 mAh g^{-1} ($Li_{1-x}CoO_2$, x=~0.63, 4.45 V vs. Li/Li^+). Increasing the charging cut-off voltage to extract more Li^+ can further increase the capacity of $LiCoO_2$ (e.g. 4.5 V vs. Li/Li^+, 6.9% increase in capacity, ~185 mAh g^{-1}; 4.6 V vs. Li/Li^+, 27.2% increase in capacity, ~220 mAh g^{-1}), however, such practice could lead to several detrimental problems,

causing rapid decay of cycle efficiency and capacity. More specifically, when the voltage reaches 4.5 V, a harmful phase transformation from O3 hexagonal phase to hybridized O1-O3 hexagonal phase (denoted as H1-3 phase. O: octahedral sites; 3: stacking sequence of oxygen layers ABCABC and 1: ABAB) occurs and is accompanied with gliding of lattice slabs and partial collapse of the O3 lattice structure[11]. Consequently, the internal strain builds up, leading to crack formation and particle pulverization[11,12]. Meanwhile, oxygen loss at high voltage further brings irreversible phase transition or even safety concerns. Besides these structural failure modes in the bulk, the surface instability is another critical issue that is amplified at the high state of charge. The high valence Co/O could trigger undesired interfacial side reactions, involving the oxidization of the electrolyte. All these factors add up to serious performance degradation of $LiCoO_2$ at high voltage, jeopardizing the practical application of the significantly increased capacity[13,14,15,16].

Many strategies have been considered to promote the cycle stability of $LiCoO_2$ at high voltage[17,18,19,20,21]. Among various approaches, foreign element doping is the most prevailing and has been demonstrated to be promising and effective for the improvement of the electrochemical performances of $LiCoO_2$[22,23,24,25]. For example, a study compared the cycle performances of doped $LiCoO_2$ at a high charging voltage of 4.5 V with various transition metal ions ($LiTM_{0.05}Co_{0.95}O_2$, TM=Mn, Fe, Cu and Zn)[26], and found that Mn doping enhanced reversible capacity the most to ~158 mAh g^{-1}, in comparison with ~138 mAh g^{-1} of bare $LiCoO_2$ after 50 cycles in the voltage

range of 3.5-4.5 V. It is also reported that concurrent doping of La, Al can greatly improve the Li diffusivity and structure stability of $LiCoO_2$[16]. With such doping strategy, $LiCoO_2$ can achieve high capacity of 190 mAh g^{-1} over 50 cycles at high cut-off voltage of 4.5 V. We point out here that, while these previous works instinctively assume that the dopants are well incorporated into parent lattice, theoretical calculations have predicted the limited solubility of foreign atoms in $LiCoO_2$ in some cases[27]. Such inconsistencies necessitate in-depth investigations of the fundamental roles of various dopants in improving the battery performances. Compared with the literature reports based on laboratory-scale experiments, it is worth noting that the doping concentration is generally 2-3 orders of magnitude lower for industrial production. Therefore, for $LiCoO_2$ with low concentration doping at a level of industrial relevance, empirical accumulation is of vital significance and the corresponding fundamental research is urgently needed. Moreover, multiple-elements co-doping is commonly executed in practice. The desired synergistic effect among multiple dopants needs further exploration, but the characterisations of multiple doping elements at low concentrations are daunting challenging.

In this work, we show that trace amount of Ti-Mg-Al co-doping (~0.1 wt% for each dopant) can greatly improve the cycle and rate performances of $LiCoO_2$ at a high charging cut-off voltage of 4.6 V. The fundamental roles of each individual dopant in promoting the electrochemical performances are systematically studied by combining various characterisations techniques including synchrotron X-ray spectroscopy and

X-ray imaging. We find that Al, Mg atoms are successfully incorporated into the $LiCoO_2$ lattice and can effectively suppress the detrimental phase transition at high charging voltage (above 4.5 V). However, even at trace amount, Ti segregates at grain boundaries and on particle surface, facilitating fast lithium diffusion and alleviating internal strain within the assembled $LiCoO_2$ particle. Moreover, the Ti-rich surface can stabilize the oxygen redox and inhibit the undesired electrode-electrolyte interfacial reactions. These experimental findings are further explained by first principles calculations, demonstrating that the extraordinary battery performances of Ti-Mg-Al co-doped $LiCoO_2$ can be attributed to both microstructure changes and electronic structure reconfiguration induced by trace amount co-doping of Ti, Mg and Al.

Characterisations of Bare-LCO and TMA-LCO

Undoped $LiCoO_2$ (Bare-LCO), Ti, Mg, Al single-element-doped $LiCoO_2$ and Ti-Mg-Al co-doped $LiCoO_2$ (TMA-LCO) were prepared using a solid-state reaction method. The inductively coupled plasma (ICP) emission spectroscopy results in Supplementary Table 1 indicate that the actual chemical compositions of these as-synthesised materials agree well with the intended compositions. Diverse characterisations of the synthesised materials were performed and the results are summarised in Supplementary Tables 2-4 and Supplementary Figs. 2-4. It is evident that foreign-atom doping has a significant influence on various aspects of the physical properties of $LiCoO_2$, such as structural parameters, particle size, morphology and

conductivity. The doping elements, especially Ti, can introduce lattice strain and slightly reduce the particle size of $LiCoO_2$. Moreover, Mg doping causes an increase in electronic conductivity, whereas Al doping has minimal impact on these physical parameters.

Here, we focus on TMA-LCO, which shows the best electrochemical performances. The Rietveld refinements of XRD patterns of Bare-LCO and TMA-LCO indicate a pure *R-3 m* layered structure with negligible differences in lattice parameters (Supplementary Fig. 2 and Supplementary Table 4). As shown in Figs. 1a and 1b, the primary particle size of TMA-LCO (D50: ~15 μm) is slightly smaller than that of Bare-LCO (D50: ~16 μm). Further elemental mappings of the local region over a TMA-LCO particle demonstrate an overall homogeneous distribution of the foreign elements Ti, Mg and Al (Fig. 1d) except for the Ti-rich edge region. In view of the resolution limit of elemental mapping, energy-dispersive X-ray spectroscopy (EDS) and electron energy loss spectroscopy (EELS) measurements were carried out, revealing the slight differences in elemental concentration between the centre and edge areas of TMA-LCO particle. As highlighted in Figs. 1e and 1f, both EDS and EELS results show that Ti has a higher elemental concentration at the surface than in the interior of the particle but there is no evident difference for Mg and Al. To further confirm this phenomenon, elemental distribution near the particle edge in a finer area was analyzed. The high-angle annular dark-field (HAADF) image and elemental mappings near the particle edge of the cross-sectional TEM sample are shown in

Supplementary Fig. 5, which demonstrate Ti aggregation at particle surface. X-ray photoelectron spectroscopy (XPS) etching results further confirm the heterogeneity of the spatial distribution of Ti within the particles (Supplementary Fig. 6).

Electrochemical performances

The electrochemical performances of Bare-LCO and TMA-LCO were evaluated in both half-cells and full-cells, and the results are displayed in Figs. 2a-2e and Supplementary Figs. 7 and 8 (initial charge-discharge curves and cycle/rate performances respectively). It is apparent that TMA-LCO presents improved cycle stability in half-cell compared with Bare-LCO, in particular at high charging cut-off voltage of 4.6 V. A high reversible discharge capacity of 174 mAh g^{-1}, with capacity retention of 86% (compared with the 2nd cycle), is achieved in TMA-LCO after 100 cycles at a current rate of 0.5C (1C = 274 mA g^{-1}, note that all cells were cycled at 0.1C for formation process at the 1st cycle). The Coulombic efficiency (CE) was also recorded during electrochemical cycling. The TMA-LCO cell shows slightly higher CE (93.7%) than Bare-LCO cell (90.2%) at 4.6 V charging for the 1st cycle, and quickly increases to 99% after 3 cycles and remains stable for the subsequent cycles (Supplementary Fig. 9). The charge-discharge profiles at selected cycle numbers are presented in Figs. 2b and 2c. It can be seen that Bare-LCO has significantly degraded voltage profiles after 50 cycles, indicating the severer structural degradation in Bare-LCO than TMA-LCO. The cycle and rate performances of single-element-doped $LiCoO_2$ were also evaluated and the results are shown in Supplementary Fig. 8. They

all show better cycle and rate performances than Bare-LCO but inferior to TMA-LCO.

For potential practical applications, full pouch cells (~2.8 Ah) with Bare-LCO or TMA-LCO cathodes and commercial graphite anodes were assembled and cycled at room temperature in the voltage range of 3.0-4.55 V (equivalent to 4.6 V vs. Li/Li^+). As shown in Fig. 2d, the capacity of Bare-LCO fades quickly to 51.3 mAh g^{-1} after 70 cycles. In contrast, the TMA-LCO cell shows much improved capacity retention with a capacity of 178.2 mAh g^{-1} after 70 cycles and much more stable CE than that of Bare-LCO (Supplementary Fig. 10). The discharge voltage remains almost unchanged at around 3.90 V for TMA-LCO, while it gradually drops to 3.51 V for Bare-LCO. The seriously degraded cycle performance of Bare-LCO full-cell can be attributed to the irreversible structural transformation and unwanted side reactions, which can be further proved by the obvious gas generation in cycled pouch cell as shown in inset of Fig. 2e. Overall, TMA-LCO shows much improved electrochemical performances in both half-cell and full-cell at a high charging cut-off voltage of 4.6 V (vs. Li/Li^+) compared with Bare-LCO (comparison of the performances with literature reports for high voltage $LiCoO_2$ are summarized in Supplementary Tables 5-6).

Structural evolution during 1st charge-discharge process

As the cycle stability of $LiCoO_2$ is strongly associated with its structural evolution, *in situ* XRD experiments were performed to study the phase transition behaviour.

Although pristine Bare-LCO and TMA-LCO share a similar crystal structure, distinct differences in structural evolution over the first charge-discharge process can be observed as shown in Figs. 3a and 3b. The (003) and (107) diffraction peaks are selected for demonstration. A relatively small (003) peak shift is observed in TMA-LCO at high voltage 4.6 V, in contrast to the dramatic (003) peak shift in Bare-LCO. This could be attributed to the suppressed O3 to H1-3 phase transition which is accompanied with the oxygen stacking sequence change (Fig. 3d)[28, 29]. Such mitigation of structural changes is also demonstrated in the (107) peak shift as highlighted by the vertical dotted lines in Figs. 3a and 3b. The (107) peak splitting at 4.1 V occurs in both Bare-LCO and TMA-LCO, which can be attributed to an order-disorder transition[30, 31]. Considering the superior battery performances of TMA-LCO, the conversion between the hexagonal and monoclinic phases at around 4.1 V may not be the main cause for performance degradation. The phase transition behaviour also manifests itself in the charge-discharge voltage profiles and cyclic voltammetry (CV) curves of Bare-LCO and TMA-LCO, which are shown in Fig. 3c. The persistence of the anodic and cathodic peaks due to the order-disorder transition and the difference between Bare-LCO and TMA-LCO at a high voltage of 4.6 V are consistent with the *in situ* XRD results.

3D elemental distributions in TMA-LCO particle

Considering the indication of a non-uniform dopant distribution from the EDS and EELS results, it is necessary to determine the actual spatial distribution of the key

elements in the $LiCoO_2$ particles. X-ray fluorescence mapping, which is capable of detecting the spatial elemental distribution and concentration with high sensitivity, was utilised to probe the 3D elemental distribution within an arbitrarily selected TMA-LCO particle. Because Mg was outside of the working energy window, only Al, Co and Ti signals were collected and the 3D renderings of their distributions are displayed in Figs. 4a-4c. Figs. 4d-4f show the elemental distributions over a virtual x-z slice through the centre of the particle. The absolute concentrations of these elements are very different as indicated by the coloured scale bar in the corresponding insets. It is evident from Figs. 4a and 4d that Al is homogeneously distributed throughout the entire particle with a minor degree of concentration variation. The Ti distribution presented in Figs. 4c and 4f, on the other hand, shows a large degree of segregation. The Ti-rich phase forms a complex interconnected network (as highlighted by the dashed lines in Fig. 4f), dividing the $LiCoO_2$ particle into several subdomains. For further evaluation of the subdomain separation effect, we first calculated the Ti to Co ratio voxel by voxel throughout the entire 3D volume. Areas with Ti: Co ratio equal to or below the nominal value are segmented as active subdomains. As shown in Fig. 4g, a total number of 50 subdomains were identified and visualised. Note that different colours are used to distinguish adjacent subdomains for visualisation. However, colours are reused for subdomains that are far apart due to the large number of subdomains identified. Further quantification of these subdomains suggests that they have a wide distribution in volume and surface area, as indicated by Figs. 4h and 4i. Compared with the entire particle as a whole, the

237 subdomains with largely reduced size and significantly increased surface area ensure
238 fast Li^+ diffusion in the micro-sized particles, which could be one major factor
239 responsible for the improved rate performance of TMA-LCO. In addition, the
240 subdomains separated by the Ti-rich phase can effectively reduce the lattice breathing
241 induced by Li intercalation and are more robust against lattice strain and particle
242 fracture, thereby possibly enhancing the long-term cycle stability of TMA-LCO. To
243 ensure the representativeness of the conclusion drawn from the single particle analysis,
244 we conducted two-dimensional (2D) elemental mapping over many TMA-LCO
245 particles using synchrotron based micro-probe. The correlation evaluation and the
246 principle component analysis (PCA) of the Co and Ti maps further confirm the
247 heterogeneity distribution of Ti from a statistical point of view (Supplementary Fig.
248 11).
249
250 **Surface reaction probed by soft X-ray spectroscopy**
251 Soft X-ray spectroscopy measurements were performed to study the surface
252 properties of Bare-LCO and TMA-LCO[32]. Considering the strong correlation between
253 oxygen involvement and battery failure at high voltage, the O-*K* edge spectra are the
254 research focus. Note that the strong hybridisation between TM *3d* and O *2p* states
255 makes it challenging to separate out the lattice oxygen signal from O-*K* edge X-ray
256 absorption spectroscopy (XAS)[33]. As a result, resonant inelastic X-ray scattering
257 (RIXS, probing depth: ~150 nm), with extra resolution along the emission energy
258 dimension, was selected as the tool-of-choice to clarify the role of oxygen[34].

O-*K* edge RIXS maps for Bare-LCO and TMA-LCO charged to 4.6 V are shown in Figs. 5a and 5b, respectively, and the corresponding RIXS maps for pristine materials are shown in Supplementary Fig. 12. Upon deep delithiation, the most obvious change for Bare-LCO is the appearance of a well-distinguished isolated feature at an incident energy of 531 eV (Fig. 5a), indicating the oxidization of O^{2-} to a higher valence state[35]. This RIXS feature becomes much weaker in TMA-LCO, indicating less participation of oxygen redox in the outer shell of TMA-LCO particles (in view of the probing depth of ~150 nm) compared with Bare-LCO, and the improved oxygen stability will also contribute to the enhanced safety behaviours at high voltage (Supplementary Figs. 13-14). Moreover, the RIXS spectra demonstrate the superior stability of TMA-LCO after 20 cycles compared with Bare-LCO, as shown in Fig. 5c. The elemental doping likely changes the intrinsic electronic structure and consequently affects the redox reactions, particularly the oxygen redox chemistry.

The route of surface reactions with electrolyte may also be affected due to the different chemical reactivity of surface oxygen between Bare-LCO and TMA-LCO. Both XPS and sXAS results confirm the distinct cathode/electrolyte interphase (CEI) formed on Bare-LCO and TMA-LCO. As can be seen from the fitted O 1s XPS spectra in Fig. 5d, lattice oxygen (shaded area) demonstrates a sharper peak that overwhelms signals from the CEI components in TMA-LCO compared with Bare-LCO, implying a relatively thinner and more stable CEI layer on TMA-LCO as

schematically illustrated in Fig. 5e. Such an interpretation is also supported by quantitative analysis of XPS results as shown in Supplementary Figs. 15 and 16 and Supplementary Table 7. Meanwhile, sXAS data collected in total electron yield (TEY) and total flourescence yield (TFY) modes can provide further contrast between surface and bulk regions. Surface-sensitive TEY and bulk-sensitive TFY signals of TMA-LCO and Bare-LCO in different cycle states are displayed as solid and dotted lines, respectively, in Supplementary Fig. 17. Note that the TEY spectra do not simply reproduce the TFY spectra, which can be attributed to interfacial reactions between the electrode and the electrolyte. The relatively low pre-edge shoulder in TEY indicates the decrease of high valence Co at the particle surface, particularly for TMA-LCO. This phenomenon implies that different types of CEI layer form on TMA-LCO and Bare-LCO, which is consistent with the O 1s XPS results. The stable interface layer between cathode materials and electrolyte can also suppress Co dissolution process (Supplementary Figs. 18-20). Therefore, the thinner and more stable CEI layer is expected to contribute to the superior electrochemical performances of TMA-LCO.

DFT calculations and doping mechanism

As Ti is rich on surface of TMA-LCO, first principles calculations were conducted to gain fundamental understandings of the Ti surface doping mechanism in $LiCoO_2$. In order to verify the experimental observations on Ti-distribution, the optimised $LiCoO_2$ (104) slab model was used (Fig. 6a). We first considered replacing one Co

atom from different layers of the slab with Ti atom and compared the total ground state energies of Ti-doped $LiCoO_2$ at different atomic layers, as listed in Supplementary Table 8. Ti atom prefers to stay at the surface layer rather than in the inner layers, with a 0.7 eV lower total energy. Then, replacing two Co atoms at the surface layer with two Ti atoms and consider the distribution of Ti atoms at the surface region. The different distances between the nearest Ti atoms on the (104) surface are shown in Supplementary Fig. 21 and the total energies are listed in Supplementary Table 9. All results indicate the preference of Ti occupancy at the surface region. The incorporation of Ti into the $LiCoO_2$ lattice alters the electronic structure as well. Fig. 6b compares the *2p* states of the O atoms at the $LiCoO_2$ (104) surface. Unoccupied O *2p* states can be observed for the surface O atoms for both Ti-doped and undoped $LiCoO_2$ in the delithiated $Li_{0.29}CoO_2$ state. However, the unoccupied states above the Fermi level are significantly suppressed after Ti doping, indicating suppressed charge deficiency in the surface layer. Fig. 6c displays the relaxed structure of delithiated $Li_{0.29}CoO_2$ together with the charge density of the surface O atoms compared with lithiated $LiCoO_2$. The charge density contour clearly shows that a substantial charge deficiency for the O atoms in the surface layer. The O atoms near the Ti atoms lose less charge compared with those far from the Ti atoms. Fig. 6d shows the optimised atomic structure of Ti-doped $Li_{0.29}CoO_2$, where Ti atoms tend to stay in the surface layer. Charge analysis shows that the surface O atoms around Ti atoms hold more charge (less oxidized), implying that Ti doping helps to resist the charge deficiency of the O atoms upon delithiation. This agrees well with

the aforementioned RIXS results.

Conclusions

In summary, by virtue of Ti-Mg-Al co-doping, the physical properties of $LiCoO_2$, including bulk crystal structure, electronic structure, particle shape and microstructure, are effectively modified. Each doping element plays a different role in modifying the material properties from different aspects. More specifically, Mg and Al atoms have been successfully doped into the $LiCoO_2$ lattice, altering the phase transition behaviour in the de/lithiation process. Mg doping can also increase the electronic conductivity of the material. In contrast, even trace amount of Ti cannot be completely incorporated into the $LiCoO_2$ lattice. The segregation of Ti at grain boundaries and on surface, on one hand, modifies the microstructure of the sample particle that is favourable for overall lithium diffusion and uniform internal strain distribution, and on the other hand, inhibits the oxygen activity and stabilizes the surface at high charging voltage. All of these effects synergistically add up to the remarkably improved electrochemical performances.

It can be inferred from this work that the rational design of electrode materials relies on comprehensive modifications from various aspects. Multi-scale and multi-faceted characterisations are the key to gain insights into the roles of the modification elements as well as the fundamental principles of the modification approaches. Moreover, as verified in this specific case, the low solubility of Ti and,

thus, the segregation at the particle surface and grain boundaries plays a vital role in electrochemical performances enhancement. The specific behaviour of Ti, which is beyond the conventional doping scenario, implies the necessity to revisit elements with a non-optimal solubility as dopants for material design and optimisation. This would have profound implications for the design of electrode materials, well beyond the present case of high voltage $LiCoO_2$ cathode for LIBs. Finally, it should be pointed out that, from the perspective of practical applications, the performances of $LiCoO_2$ at 4.6 V is still far from satisfactory. The development of high energy density LIBs with high voltage $LiCoO_2$ requires comprehensive consideration of cathode, anode, electrolyte and other key components, which calls for more research efforts and engineering considerations. Nonetheless, this work unfolds the promising future of dragging $LiCoO_2$ to even higher voltage and approaching the theoretical capacity limit for practical applications.

Methods

Material synthesis. The $LiCoO_2$ materials were prepared by a solid-state reaction method using Li_2CO_3 (99%), Co_3O_4 (99.7%), Al_2O_3 (99.9%), MgO (99%) and TiO_2 (99.9%) as precursors. All of the raw materials are industrial materials with battery grade. An excess of 5 wt% Li_2CO_3 was used to compensate for the lithium loss during high temperature synthesis. The starting materials were ground in an agate mortar and the mixed powders were sintered at 1000 □ for 10 h in an alumina crucible to form the intermediate products. Then the intermediate products were ground again in an

agate mortar and sintered for the second time at 900 □ for 10 h to get the final products.

XRD and SEM characterisation. The XRD measurements were conducted by using a Bruker D8 Advance diffractometer with Cu-Kα radiation (λ= 1.5405 Å) in the scan range (2θ) of 10^{o}-80^{o}. For the *in situ* XRD experiments, a specially designed Swagelok cell equipped with an X-ray-transparent aluminum window was used for the *in situ* measurements. The *in situ* XRD patterns were collected with an interval of 40 min for each 2θ scan from 10^{o} to 60^{o} on charging and discharging at a current rate of 0.1C (1C= 274 mA g^{-1}). The morphologies of the samples were investigated by a scanning electron microscopy (SEM, Hitachi-S4800).

XPS characterisation. The X-ray photoelectron spectroscopy (XPS) were recorded with a spectrometer having Mg/Al Kα radiation (ESCALAB 250 Xi, ThermoFisher). All binding energies were calibrated using the C 1s peak of the Super P at 284.4 eV as an internal standard. In order to prevent the air exposure, all samples were transferred by using a transfer box provided by ThermoFisher.

TEM characterisation. The TEM/STEM images, EDS, and EELS measurements were performed by using a JEOL ARM200F microsocpe operating at 200 kV, which is equipped with a probe-forming aberration corrector and Gatan image filter (GIF Quantum 965).

Half-cell assembly. The $LiCoO_2$/Li half-cell tests were conducted using coin cells (CR2032), assembled in an argon filled glove-box. The working electrodes were prepared by coating the mixture slury of active material (80 wt%), super P (10 wt%)

391 and poly-vinylidene fluoride (PVDF, 10 wt%) on aluminum current collector,
392 followed by drying at 120 ^{o}C in vacuum for 10 h. The loading of active material was
393 controlled to between 3.0-4.0 mg cm^{-2}. The electrolyte was a solution of 1 M $LiPF_6$ in
394 ethylene (EC) and dimethyl carbonate (DMC) (1 :1 in volume). Lithium foil was used
395 as the counter electrode and Al_2O_3 coated polyethylene (PE) film was used as the
396 separator.

397 **Full-cell assembly.** The $LiCoO_2$/Graphite full-cell tests were conducted using stacked
398 pouch cells, assembled in a dry room. The cathode electrodes were prepared by
399 coating the mixture slurry of active material (95 wt%), carbon black (3 wt%) and
400 poly-vinylidene fluoride (PVDF, 2 wt%) on aluminum current collector, followed by
401 drying at 120 ^{o}C in vacuum for 10 h. The areal capacity was controlled to between
402 3.5-3.8 mAh cm^{-2}. The anode electrodes are composed of graphite (94.5 wt%), carbon
403 black (2 wt%), carboxy methyl cellulose sodium (CMC-Na, 1.5 wt%) and styrene
404 butadiene rubber (SBR, 2 wt%), fabricated following the same coating and drying
405 procedures. The capacity ratio between negative electrode and positive electrode (N/P)
406 was controlled to between 1.05-1.08. The electrolyte and separator were the same as
407 those used in half-cells.

408 **Electrochemical measurements.** The charge and discharge tests were carried out
409 using a Land CT2001A battery test system (Wuhan, PR China) in a voltage range of
410 3.0-4.6 V at various C-rates at room temperature for half-cells. For the full-cell tests, a
411 constant current and constant voltage (CCCV) mode was used. The cells were charged
412 at 0.33C to 4.55 V and then held until the current drops to 0.1C. The discharge

process was conducted at constant current mode at 0.33C. The full-cells were cycled at the first two cycles for the formation process. For the first cycle, the pouch cells were charged at 0.02C for 2 h. After resting for 5 minutes, the cells were charged at 0.2C to 4.55 V and then held at the voltage until the current dropped to 0.02C (constant voltage process). Then, the cells were discharged at 0.2C to 3 V and rest for 5 minutes. For the second cycle, the cells were charged at 0.2C to 3.85 V and rest at 45 ^{o}C for 48 h to complete the formation process.

Synchrortron 2D/3D fluorescence measurement and data analysis. Nano and micro fluorescence mapping was performed, respectively, at the Hard X-ray Nano-probe (HXN) Beamline of the National Synchrotron Light Source II at Brookhaven National Laboratory (NSLS-II, BNL) and the Beamline 2-3 of Stanford Synchrotron Radiation Lightsource at SLAC National Accelerator Laboratory (SSRL, SLAC). The nano probe experiment was carried out at 9.6 keV by focusing the coherent monochromatic X-rays down to a 50 nm spot size using a Fresnel X-ray zone plate. Tomography measurement was performed by collecting a total of 51 projections from -75^{o} to 75^{o} with 3^{o} intervals. The tomographic reconstruction was carried out using an iterative algorithm known as algebraic reconstruction technique (ART). Further visualization and quantification of the imaging data were carried out using a comercial software package, Avizo. The segmentation of sub-domains in the imaged particle is based on the concentration ratio between the Co and Ti. As discussed in the main text, the regions rich in Ti form interconnected networks (Figs. 4c and 4f) that divide the particle into 50 sub-domains (Fig. 4g). Micro probe

experiment was carried out using an K-B mirror focused X-ray spot of ~1 μm to image a large field of view covering many particles to ensure the statistical representativeness (Supplementary Figure 11). The correlation analysis of Ti and Co distribution is coupled with principile component analysis to separate the Ti-rich domains from the area of the nominal composition.

Synchrotron soft X-ray spectroscopy. Soft X-ray spectroscopy measurements were performed at beamline 8.0.1 of the Advanced Light Source at Lawrence Berkeley National Laboratory (ALS, LBNL). The beamline is equipped with a spherical grating monochramator which supplies linearly polarized soft X-ray with resolving power up to 6000. The XAS spectra were collected in both TEY and TFY modes simultaneously. TEY is surface sensitive with probing depth of ~10 nm, while TFY provides bulk information with probing depth of ~150 nm. The energy of the O-*K* edge XAS spectra were aligned based on O-*K* edge of Fe_2O_3 reference. The spectra intensities were normalized to the beam flux measured by a gold mesh at upstream. The RIXS experiments were carried out with the (high-resolution RIXS) hr-RIXS system at beamline 8.0.1 in ALS. The newly build up system is equipped with a refocusing mirror, a spherical pre-mirror, a variable line spacing grating and a high resolution X-ray photon detector with entrance slitless design. The slitless operation improves the acceptance angle of the spectrograph and increases the throughput without comprising energy resolution. The incident excitation energy scale was calibrated according to XAS of Fe_2O_3 reference sample, while subsequent emission energy was calibrated using the elastically scattering line. The final data sets were presented in a

two-dimensional map, where the emission intensity was color coded as a function of the incident excitation (ordinate) energy and emission energy (abscissa).

First principles calculations. All density functional theory (DFT) calculations were performed with the Vienna ab initio simulation package (VASP)[36]. The spin-polarized generalized gradient approximation (GGA) with PBE function[37] was used to treat the electron exchange-correlation interactions, and the projector-augmented wave (PAW) approach[38] was used to take into account of the electron-ion interactions. Because GGA cannot reproduce correctly the localized electronic states of the transition metal oxide materials, GGA+U method was used[39,40]. The U values for the Co-*3d* and Ti-*3d* states were chosen to be 4.91 and 5.0 eV respectively[41,42]. Furthermore, we included the Van der Waals interaction throughout the calculations. A plane-wave basis with a kinetic energy cutoff of 520 eV was used. The Monkhorst-Pack scheme[43] with $2 \times 3 \times 1$ k-point mesh was used for the integration in the irreducible Brillouin zone. The lattice parameters and the ionic position were fully relaxed, and the final forces on all atoms are less than 0.01 eV $Å^{-1}$. The calculation of the density of states (DOS) was smeared by the Gaussian smearing method with a smearing width of 0.05 eV. The $LiCoO_2$ (104) surface was simulated by symmetric periodic slab model containing 42 Li atoms, 84 O atoms and 42 Co atoms, with consecutive slabs separated by a 18 Å vacuum layer. The delithiated state $Li_{0.29}CoO_2$ was modeled by extract 30 out of 42 Li ions from the $LiCoO_2$ slab system. The Ti-doped $LiCoO_2/Li_{0.29}CoO_2$ slab system was modeled by substituting one out of 42 Co ions by a Ti ion.

Data Availability

The data that support the plots within this paper and other finding of this study are available from the corresponding author upon reasonable request.

Acknowledgements

The work was supported by funding from National Key R&D Program of China (grant no. 2016YFB0100100), National Natural Science Foundation of China (grant no. 51822211, 11574281) and the Foundation for Innovative Research Groups of the National Natural Science Foundation of China (grant no. 51421002). The work done at BNL were supported by the Assistant Secretary for Energy Efficiency and Renewable Energy, Vehicle Technology Office of the U.S. Department of Energy through the BMR Program, including Battery 500 Consortium under contract DE-SC0012704. Use of the National Synchrotron Light Source II is supported by the U.S. Department of Energy, an Office of Science user Facility operated by Brookhaven National Laboratory under Contract No. DE-SC0012704. SLAC National Accelerator Laboratory, is supported by the U.S. Department of Energy, Office of Science, Office of Basic Energy Sciences under Contract No. DE-AC02-76SF00515. Use of the Stanford Synchrotron Radiation Lightsource, SLAC National Accelerator Laboratory, is supported by the U.S. Department of Energy, Office of Science, Office of Basic Energy Sciences under Contract No. DE-AC02-76SF00515. Soft X-ray spectroscopic data were collected at beamline 8.0.1 of the Advanced Light Source, which is supported by the Director, Office of Science, Office of Basic Energy

Sciences, of the U.S. Department of Energy under Contract No. DE-AC02-05CH11231. We gratefully acknowledge the help from beamline BL14W1 and BL08U at Shanghai Synchrotron Radiation Facility (SSRF, China).

Author's contribution

X.Y. and H.L. conceived the idea; J.N.Z. synthesized the materials and performed electrochemistry measurements and X-ray diffraction measurements; C.M. performed TEM measurements and analysis; Y.L., M.G., X.H., S.L. and Y.C. performed TXM measurement and data analysis; Q.L. and W.Y. performed the soft X-ray spectroscopy experiment and data analysis; O.C. and R.X. performed DFT analysis; Q.L., X.Y., J.N.Z., Y.L. and O.C. wrote the paper with critical inputs from all other authors; X.Y., Y.L. and H.L. edited and finalized the manuscript.

Competing interests

The authors declare no competing interests.

References:

1. Whittingham, M. S. Ultimate limits to intercalation reactions for lithium batteries. *Chem. Rev.* **114,** 11414-11443 (2014).

2. Goodenough, J. B. Evolution of strategies for modern rechargeable batteries. *Accounts Chem. Res.* **46,** 1053-1061 (2013).

3. Nitta N., Wu F., Lee J. T. & Yushin G. Li-ion battery materials: present and future. *Mater. Today* **18,** 252-264 (2015).

4. Lin F.*et al.* Metal segregation in hierarchically structured cathode materials for high-energy

lithium batteries. *Nat. Energy.* **1,** 15004 (2016).

5. Lin F. *et al.* Surface reconstruction and chemical evolution of stoichiometric layered cathode materials for lithium-ion batteries. *Nat. Commun.* **5,** 3529 (2014).

6. Liu C. F., Neale Z. G. & Cao G. Z. Understanding electrochemical potentials of cathode materials in rechargeable batteries. *Mater. Today* **19,** 109-123 (2016).

7. Wang D. W. *et al.* Synthetic control of kinetic reaction pathway and cationic ordering in high-Ni layered oxide cathodes. *Adv. Mater.* **29,** 1606715 (2017).

8. Radin M. D. *et al.* Narrowing the gap between theoretical and practical capacities in Li-ion layered oxide cathode materials. *Adv. Energy. Mater.* **7,** 1602888 (2017).

9. Kalluri S. *et al.* Surface engineering strategies of layered $LiCoO_2$ cathode material to realize high-energy and high-voltage Li-ion cells. *Adv. Energy. Mater.* **7,** 1601507 (2017).

10. Run Gu. *et al.* Improved electrochemical performances of $LiCoO_2$ at elevated voltage and temperature with an in situ formed spinel coating layer. *ACS Appl. Mater. Inter.* **10,** 31271−31279 (2018).

11. Yano A., Shikano M., Ueda A., Sakaebe H. & Ogumi Z. $LiCoO_2$ degradation behavior in the high-voltage phase transition region and improved reversibility with surface coating. *J. Electrochem. Soc.* **164,** A6116-A6122 (2017).

12. Xu Y. H. *et al.* In situ visualization of state-of-charge heterogeneity within a $LiCoO_2$ particle that evolves upon cycling at different rates. *ACS Energy Lett.* **2,** 1240-1245 (2017).

13. MacNeil D. D. & Dahn J. R. The reactions of $Li_{0.5}CoO_2$ with nonaqueous solvents at elevated temperatures. *J. Electrochem. Soc.* **149,** A912-A919 (2002).

14. Doh C-H. *et al.* Thermal and electrochemical behaviour of C/Li_xCoO_2 cell during safety test. *J. Power Sources* **175,** 881-885 (2008).

15. Whittingham M. S. Lithium batteries and cathode materials. *Chem. Rev.* **104,** 4271-4301 (2004).

16. Liu Q. *et al.* Approaching the capacity limit of lithium cobalt oxide in lithium ion batteries via lanthanum and aluminium doping. *Nat. Energy* **3**, 936-943 (2018).

17. Lu Y-C., Mansour A. N., Yabuuchi N. & Shao-Horn Y. Probing the origin of enhanced stability of "$AlPO_4$" nanoparticle coated $LiCoO_2$ during cycling to high voltages: combined XRD and XPS studies. *Chem. Mater.* **21,** 4408-4424 (2009).

18. Kalluri S. *et al.* Feasibility of cathode surface coating technology for high-energy lithium-ion and beyond-lithium-ion batteries. *Adv. Mater.* **29,** 1605807 (2017).

19. Wu N., Zhang Y., Wei Y., Liu H. & Wu H. Template-engaged synthesis of 1D hierarchical chainlike $LiCoO_2$ cathode materials with enhanced high-voltage lithium storage capabilities. *ACS Appl. Mater. Inter.* **8,** 25361-25368 (2016).

20. Wang F. *et al.* Stabilizing high voltage $LiCoO_2$ cathode in aqueous electrolyte with interphase-forming additive. *Energ. Environ. Sci.* **9,** 3666-3673 (2016).

21. Wang J., Ji Y. J., Appathurai N., Zhou J. G. & Yang Y. Nanoscale chemical imaging of the additive effects on the interfaces of high-voltage $LiCoO_2$ composite electrodes. *Chem. Commun.* **53,** 8581-8584 (2017).

22. Wang L. L., Chen B. B., Ma J., Cui G. L. & Chen L. Q. Reviving lithium cobalt oxide-based lithium secondary batteries-toward a higher energy density. *Chem. Soc. Rev.* **47,** 6505-6602 (2018).

23. Koyama Y., Arai H., Tanaka I., Uchimoto Y. & Ogumi Z. First principles study of dopant solubility and defect chemistry in $LiCoO_2$. *J. Mater Chem. A* **2,** 11235-11245 (2014).

24. Gopukumar S., Jeong Y. & Kim K B. Synthesis and electrochemical performance of tetravalent doped $LiCoO_2$ in lithium rechargeable cells. *Solid State Ionics* **159**, 223-232 (2003).

25. Tukamoto H. & West A. R. Electronic conductivity of $LiCoO_2$ and its enhancement by magnesium doping. *J. Electrochem. Soc.* **144**, 3164-3168 (1997).

26. Zou M., Yoshio M., Gopukumar S. & Yamaki J. Synthesis of high-voltage (4.5 V) cycling doped $LiCoO_2$ for use in lithium rechargeable cells. *Chem. Mater.* **15,** 4699-4702 (2003).

27. Kim S. *et al.* Self-assembly of core-shell structures driven by low doping limit of Ti in $LiCoO_2$: first-principles thermodynamic and experimental investigation. *Phys. Chem. Chem. Phys.* **19,** 4104-4113 (2017).

28. Van der Ven A., Aydinol M. K., Ceder G., Kresse G. & Hafner J. First-principles investigation of phase stability in Li_xCoO_2. *Phys. Rev. B* **58,** 2975-2987 (1998).

29. Amatucci G. G., Tarascon J. M. & Klein L. C. CoO_2, the end member of the Li_xCoO_2 solid solution. *J. Electrochem. Soc.* **143,** 1114-1123 (1996).

30. Reimers J. N. & Dahn J. R. Electrochemical and In situ X-Ray diffraction studies of lithium intercalation in Li_xCoO_2. *J. Electrochem. Soc.***139,** 2091-2097 (1992).

31. Yang S-H., Levasseur S., Weill F. & Delmas C. Probing lithium and vacancy ordering in O3

layered Li_xCoO_2 ($x \approx 0.5$): an electron diffraction study. *J. Electrochem. Soc.* **150,** A366-A373 (2003).

32. Yang W. *et al.* Key electronic states in lithium battery materials probed by soft X-ray spectroscopy. *J. Electron Spectrosc.* **190,** 64-74 (2013).

33. Yoon W-S. *et al.* Oxygen contribution on Li-Ion intercalation-deintercalation in $LiCoO_2$ investigated by O K-Edge and Co L-Edge X-ray absorption spectroscopy. *J. Phys. Chem. B* **106,** 2526-2532 (2002).

34. Kotani A. & Shin S. Resonant inelastic x-ray scattering spectra for electrons in solids. *Rev. Mod. Phys.* **73,** 203-246 (2001).

35. Yang W. & Devereaux T. P. Anionic and cationic redox and interfaces in batteries: Advances from soft X-ray absorption spectroscopy to resonant inelastic scattering. *J. Power Sources* **389**, 188-197 (2018).

36 Kresse G. & Furthmüller J. Efficient iterative schemes for ab initio total-energy calculations using a plane-wave basis set. *Phys. Rev. B* **54,** 11169-11186 (1996).

37. Perdew J. P., Burke K. & Ernzerhof M. Generalized gradient approximation made simple. *Phys. Rev. Lett.* **77,** 3865-3868 (1996).

38. Kresse G. & Joubert D. From ultrasoft pseudopotentials to the projector augmented-wave method. *Phys. Rev. B* **59,** 1758-1775 (1999).

39. Anisimov V. I., Zaanen J. & Andersen O. K. Band theory and Mott insulators: Hubbard U instead of Stoner I. *Phys. Rev. B* **44,** 943-954 (1991).

40. Vladimir I. A., Aryasetiawan F. & Lichtenstein AI. First-principles calculations of the electronic structure and spectra of strongly correlated systems: the LDA + U method. *J. Phys-Condens. Mat.* **9,** 767 (1997).

41. Zhou F., Cococcioni M., Marianetti C. A., Morgan D. & Ceder G. First-principles prediction of redox potentials in transition-metal compounds with LDA+*U*. *Phys. Rev. B.* **70,** 235121 (2004).

42. Tanaka S. *et al.* Atomic and electronic structures of $Li_4Ti_5O_{12}/Li_7Ti_5O_{12}$ (001) interfaces by first-principles calculations. *J. Mater. Sci.* **49,** 4032-4037 (2014).

43. Monkhorst H. J. & Pack J. D. Special points for Brillouin-zone integrations. *Phys. Rev. B* **13,** 5188-5192 (1976).

Figures

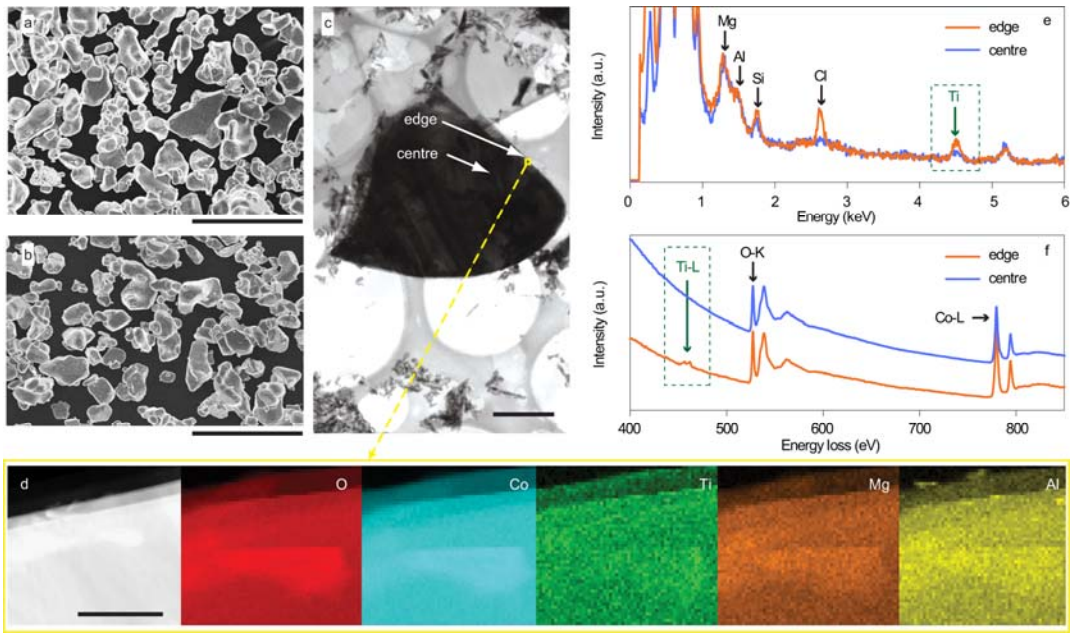

Fig. 1 Morphology and elemental distribution in Bare-LCO and TMA-LCO. SEM images of (**a**) Bare-LCO and (**b**) TMA-LCO, scale bar: 20 μm. (**c**) Cross-sectional TEM image of TMA-LCO, scale bar: 2 μm. (**d**) HADDF-STEM image and EDS elemental mappings of O, Co, Ti, Mg, and Al (scale bar: 100 nm) of the selected region indicated by the yellow rectangular in **(c)**, demonstrating an overall homogeneous distribution of the doping elements Ti, Mg and Al except for the Ti-rich edge region (see the enlarged images and integrated intensity profiles in Supplementary Fig. 5). (**e**) EDS and (**f**) EELS spectra collected separately from the edge (surface) and centre (interior) regions of TMA-LCO, as indicated by the white arrows in **(c)**. The rectangular in green colour highlights the signal of Ti, revealing the slightly increased concentration of Ti in the edge region by comparing with the centre region in the TMA-LCO particle.

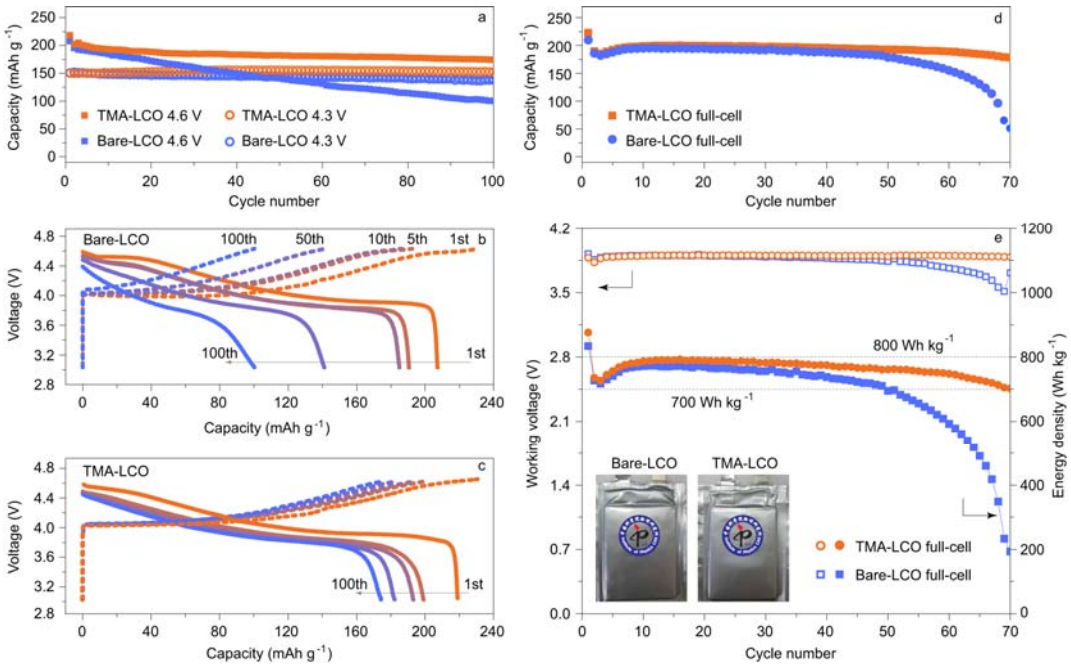

Fig. 2 Electrochemical characterisation of Bare-LCO and TMA-LCO. (**a**) Comparison of cycle performances of $LiCoO_2$|Li half-cells with Bare-LCO and TMA-LCO. Charge-discharge curves of (**b**) Bare-LCO and (**c**) TMA-LCO half-cells for 1st, 5th, 10th, 50th and 100th cycles. The charge and discharge tests were conducted at 0.1C for the 1st cycle and 0.5C for the subsequent cycles. (**d**) Cycle performances of $LiCoO_2$|Graphite full-cells with Bare-LCO and TMA-LCO. A CCCV mode was used for the full-cell tests. For the charge process, the cells were charged at 0.33C to 4.55 V and then held the voltage until the current dropped to 0.1C. The discharge current was 0.33C. (**e**) The discharge voltage of the full-cells and energy density of cathode materials as a function of cycle number. The inset shows the pouch cells after 70th cycle and obvious gas generation can be observed in the Bare-LCO|Graphite pouch cell.

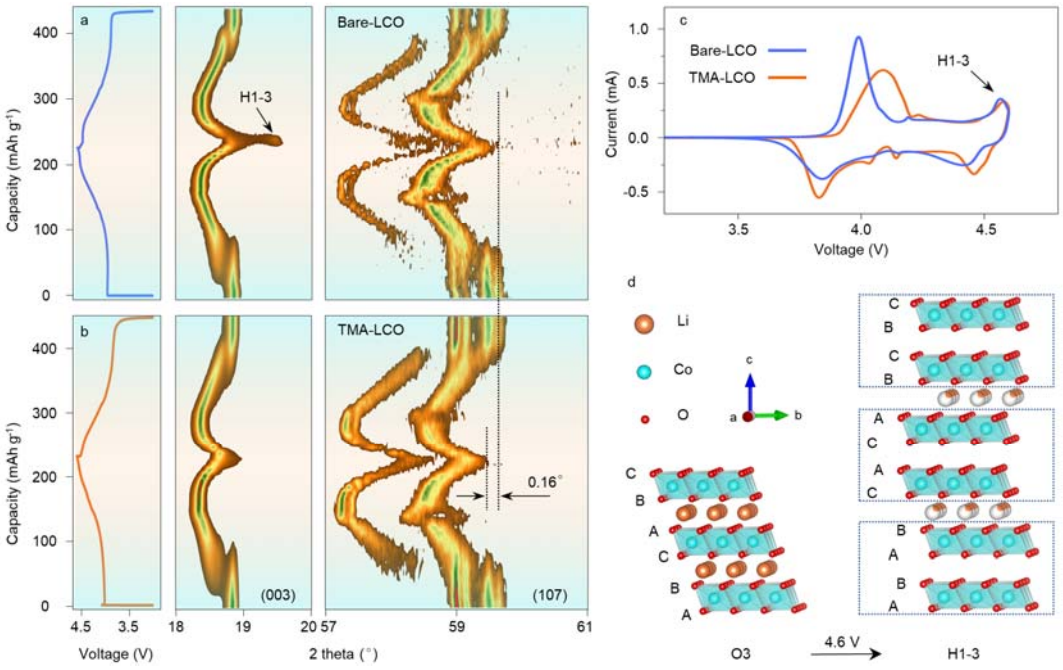

688

689 **Fig. 3 Structural evolution during initial charge-discharge process.** *In situ* XRD

690 evolution of (**a**) Bare-LCO and (**b**) TMA-LCO at the (003) and (107) diffraction

691 peaks, with the corresponding charge-discharge curves aligned to the left. A

692 suppressed O3 to H1-3 phase transition with smaller (107) diffraction peak shift

693 (0.16^{o}) can be observed in TMA-LCO at 4.6V charged state. (**c**) Cyclic voltammetry

694 results of Bare-LCO and TMA-LCO. (**d**) Schematic diagrams on atomic stacking of

695 Li_xCoO_2 in the O3 and H1-3 phases. For pristine $LiCoO_2$, it can be described as O3

696 phase with oxygen layer stacking sequence of ABCABC. Upon charging to 4.6 V,

697 such sequence changes into ABABCACABCBC and the O3 to H1-3 phase transition

698 occurs.

699

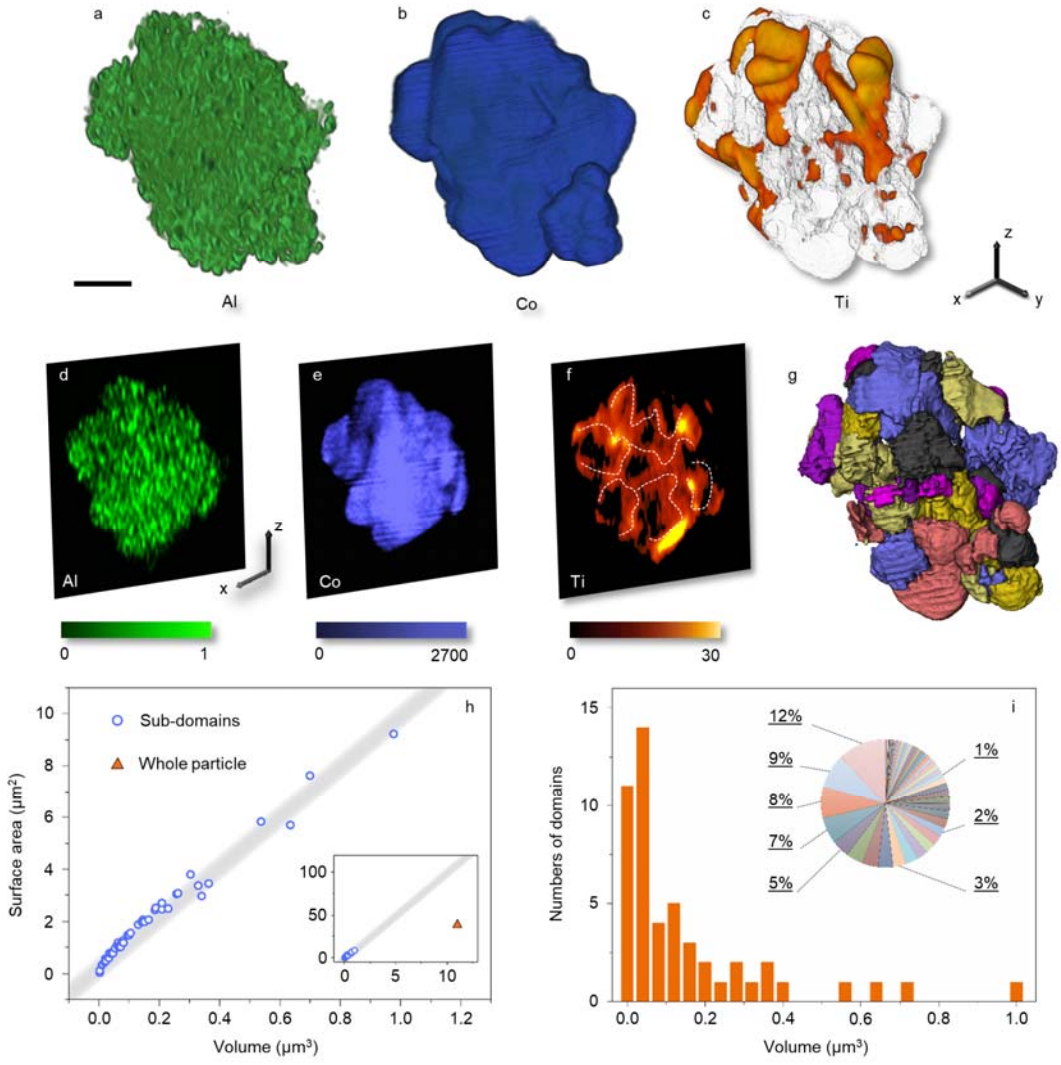

Fig. 4 3D X-ray tomography reconstruction and element distribution in TMA-LCO. 3D spatial distributions of (**a**) Al, (**b**) Co and (**c**) Ti probed by FY-STXM. Elemental distributions of (**d**) Al, (**e**) Co and (**f**) Ti over the virtual x-z slice through the centre of the particle. (**g**) Identified and visualised subdomain formation. Note that different colours are used to distinguish adjacent subdomains. (**h**) Quantification of the volume and the surface area of the sub-domains and the entire particle as a whole (see inset for a zoom-out view). The grey shadow is the linear trend extracted from

the sub-domains' data. (**i**) The volume distribution of all the sub-domains. The inset shows the volume fraction of each individual sub-domains, highlighting the existence of a few large sub-domains, which make up nearly 50% of the total volume, and a large number of small domains. The scale bar in (**a**) is 1 μm.

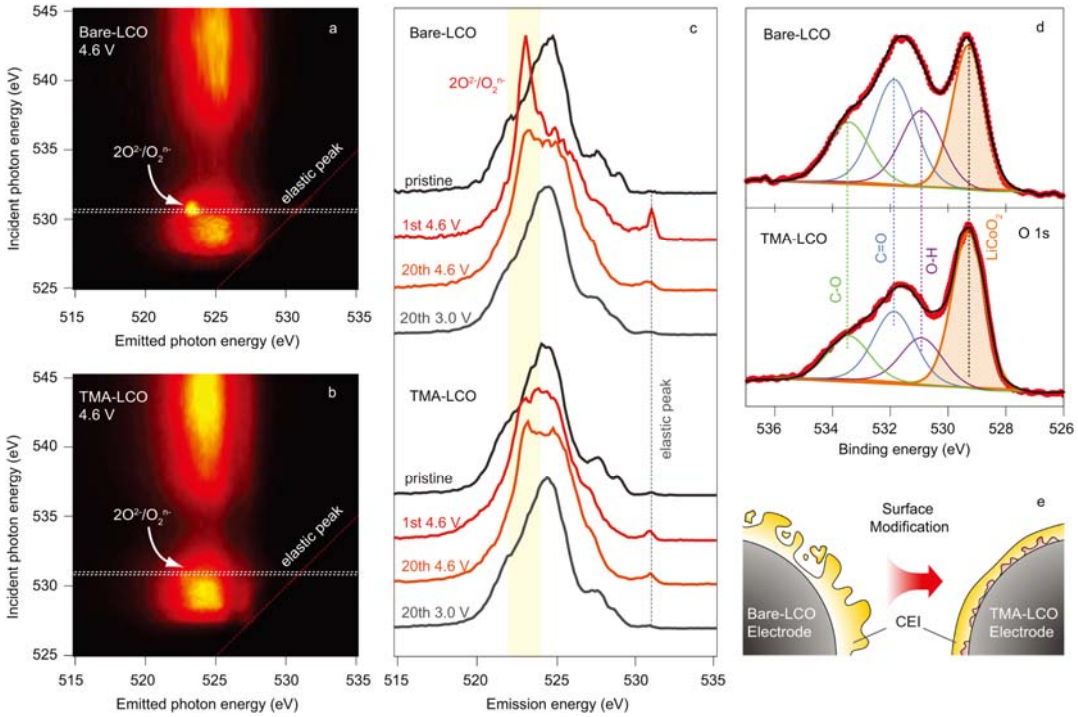

727

728 **Fig. 5 Revealing the surface chemistry by soft X-ray spectroscopy**. O-*K* edge
729 RIXS maps collected on 4.6 V charged (**a**) Bare-LCO and (**b**) TMA-LCO. With a low
730 X-ray irradiation energy of ~529 eV, O *1s* electrons get excited into unoccupied Co
731 *3d*-O *2p* hybridisation states, whereas irradiation with high-energy X-rays (~540 eV)
732 excites O *1s* electrons into Co *4sp*-O *2p* hybridisation states. (**c**) RIXS spectra
733 collected on Bare-LCO and TMA-LCO in pristine, 4.6 V charged states, and 3.0V
734 discharged state after the 20th cycles with an X-ray excitation energy of 531 eV. The
735 electrodes were prepared from cells cycled at a current rate of 0.1C. (**d**) O 1s XPS
736 spectra of Bare-LCO (top) and TMA-LCO (bottom) electrodes after the 10th cycle at
737 3.0 V discharged state. (**e**) An illustration of the differences in CEI between
738 Bare-LCO and TMA-LCO.

739

740

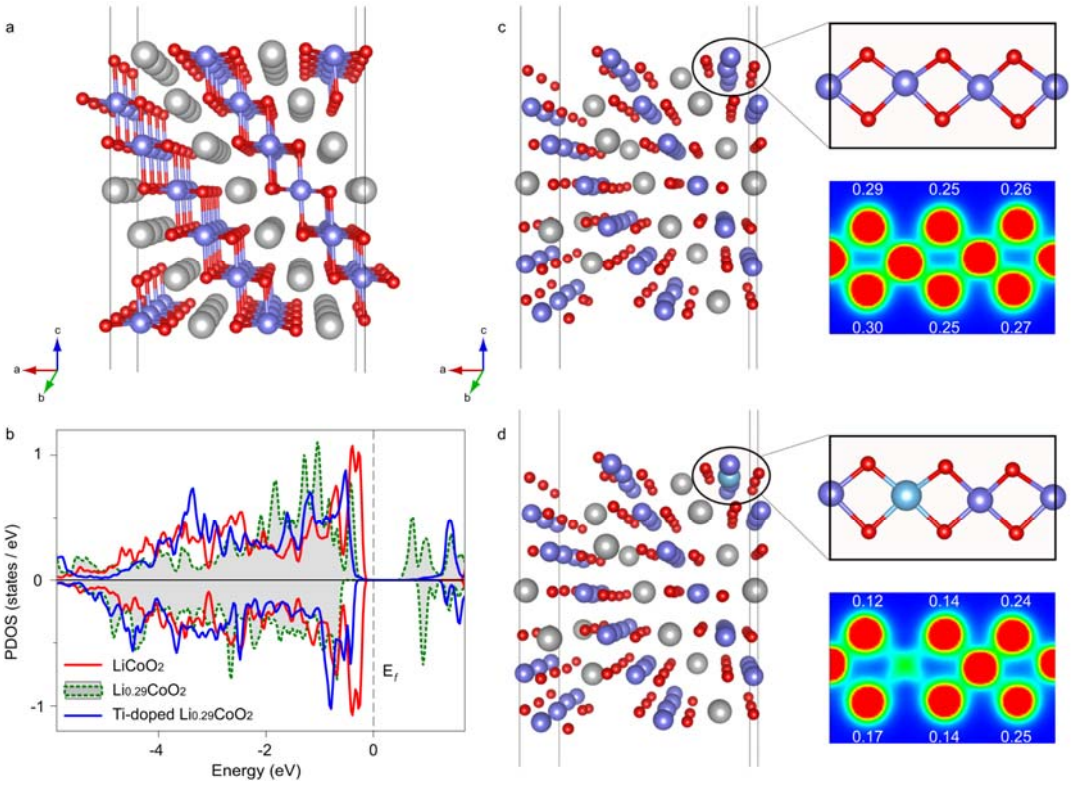

Fig. 6 DFT calculations for Ti substitution that can modify the surface electronic structure. (**a**) Optimised atomic structure of the (104) slab of $LiCoO_2$. The grey, blue and red spheres represent Li, Co and O atoms, respectively. The larger cyan sphere in (**d**) represents the Ti ion substituting the corresponding Co ion. (**b**) Projected density of states of the surface O atom at the (104) surface of $LiCoO_2$, $Li_{0.29}CoO_2$ and Ti-doped $Li_{0.29}CoO_2$. (**c**) Optimised atomic structure of the (104) slab of $Li_{0.29}CoO_2$. (**d**) Optimised atomic structure of the Ti-doped (104) slab of $Li_{0.29}CoO_2$. The insets on the right-hand side for (**c**) and (**d**) are the top views of the corresponding surface structures and the surface charge density contours, respectively. The numbers on the charge density contours are the charge loss (in electron) of the corresponding O atom upon delithiation from $LiCoO_2$ to $Li_{0.29}CoO_2$ obtained from Bader charge analysis.

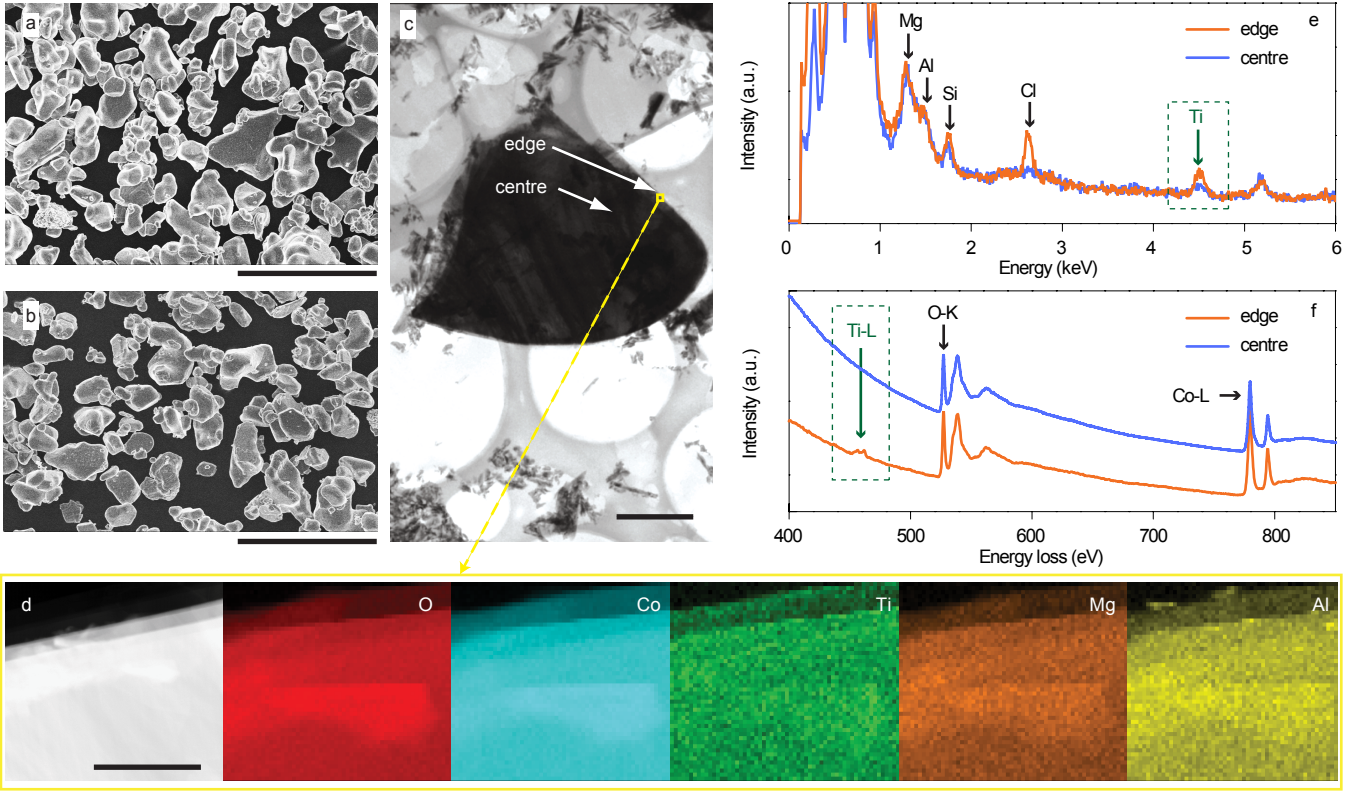
a
b
c
edge
centre
e
Mg
Al
Si
Cl
Ti
edge
centre
Intensity (a.u.)
0
1
2
3
4
5
6
Energy (keV)
f
Ti-L
O-K
Co-L
edge
centre
Intensity (a.u.)
400
500
600
700
800
Energy loss (eV)
d
O
Co
Ti
Mg
Al

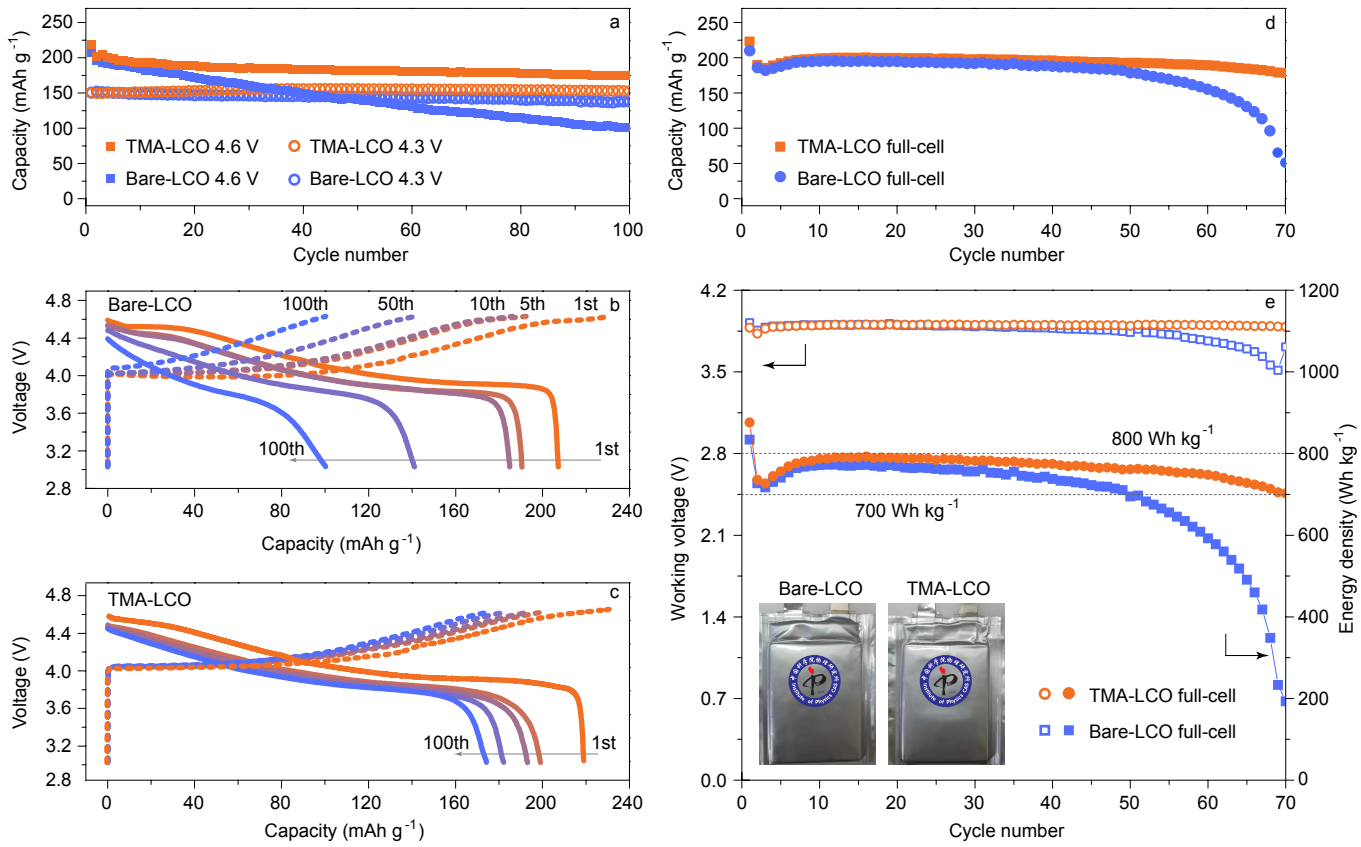
a
Capacity (mAh g-1)
Cycle number
TMA-LCO 4.6 V
TMA-LCO 4.3 V
Bare-LCO 4.6 V
Bare-LCO 4.3 V
d
Capacity (mAh g-1)
Cycle number
TMA-LCO full-cell
Bare-LCO full-cell
b
Bare-LCO
100th
50th
10th
5th
1st
Voltage (V)
Capacity (mAh g-1)
c
TMA-LCO
e
Working voltage (V)
Energy density (Wh kg-1)
800 Wh kg-1
700 Wh kg-1
Bare-LCO
TMA-LCO
TMA-LCO full-cell
Bare-LCO full-cell

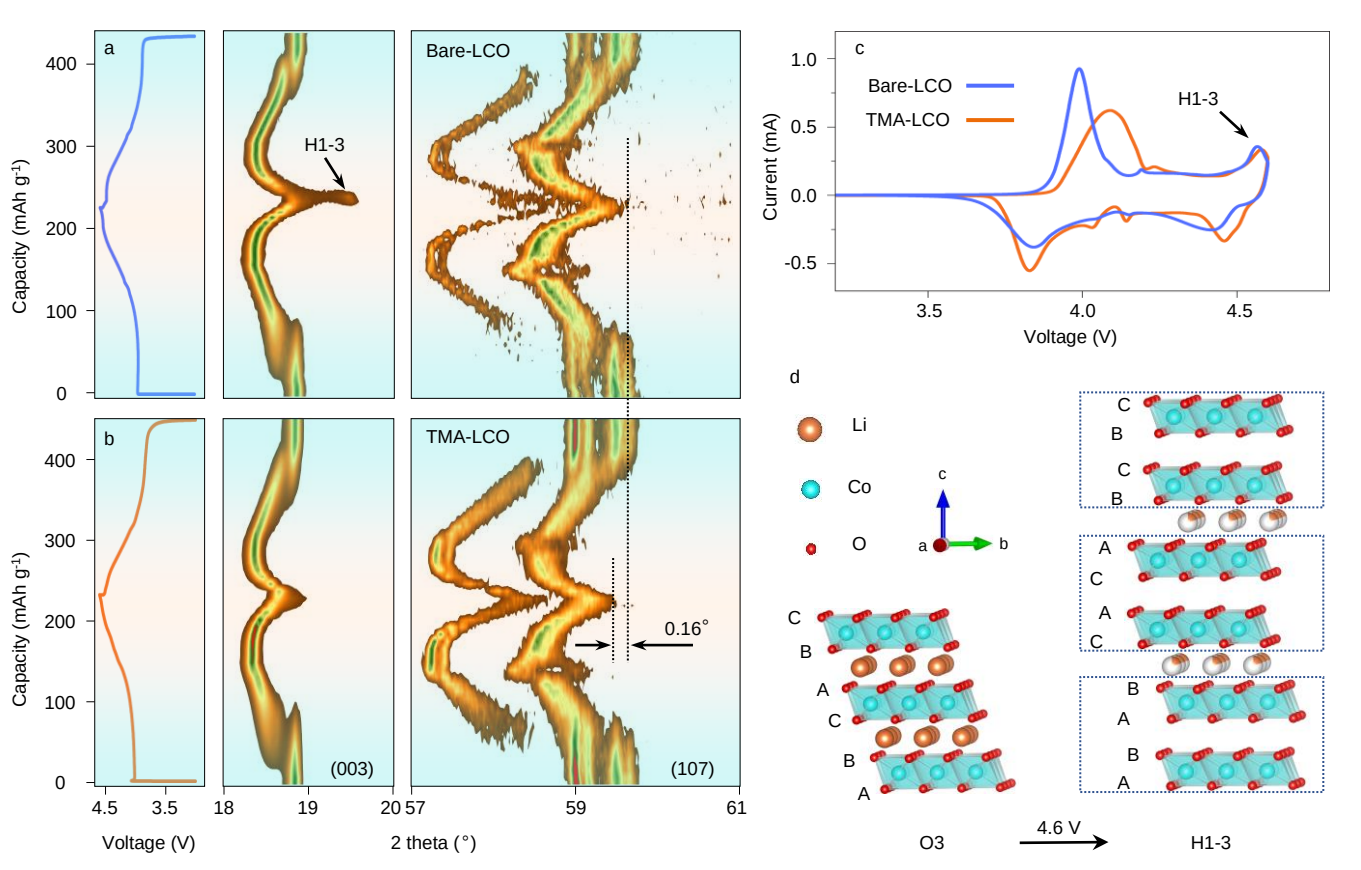
a
b
c
d
Bare-LCO
TMA-LCO
H1-3
(003)
(107)
0.16°
Capacity (mAh g-1)
Voltage (V)
2 theta (°)
Current (mA)
Li
Co
O
O3
4.6 V
H1-3

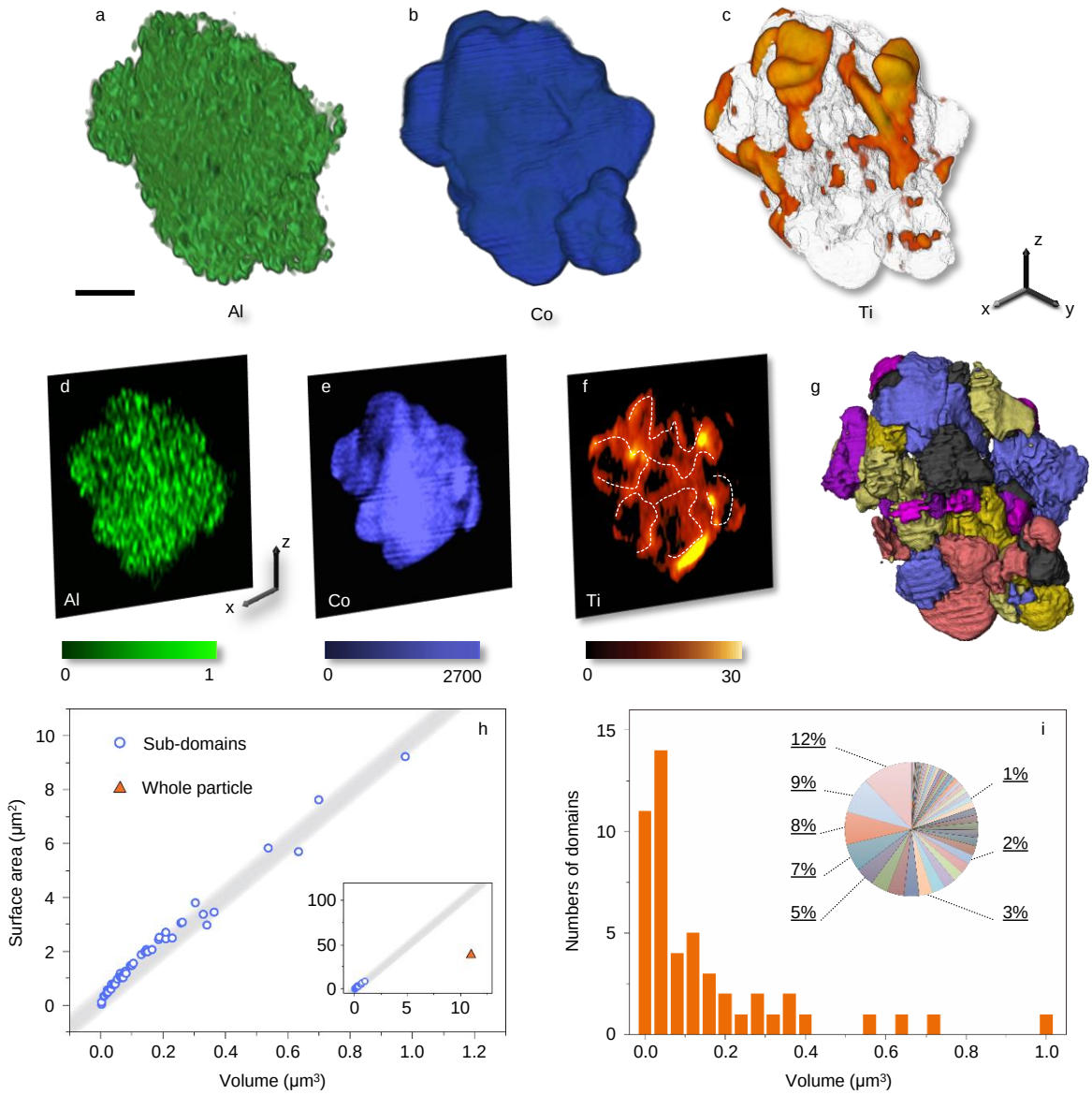
a
b
c
Al
Co
Ti
z
x
y
d
e
f
g
Al
Co
Ti
z
x
0
1
0
2700
0
30
h
Sub-domains
Whole particle
Surface area (μm²)
Volume (μm³)
i
Numbers of domains
Volume (μm³)
12%
1%
9%
2%
8%
7%
5%
3%

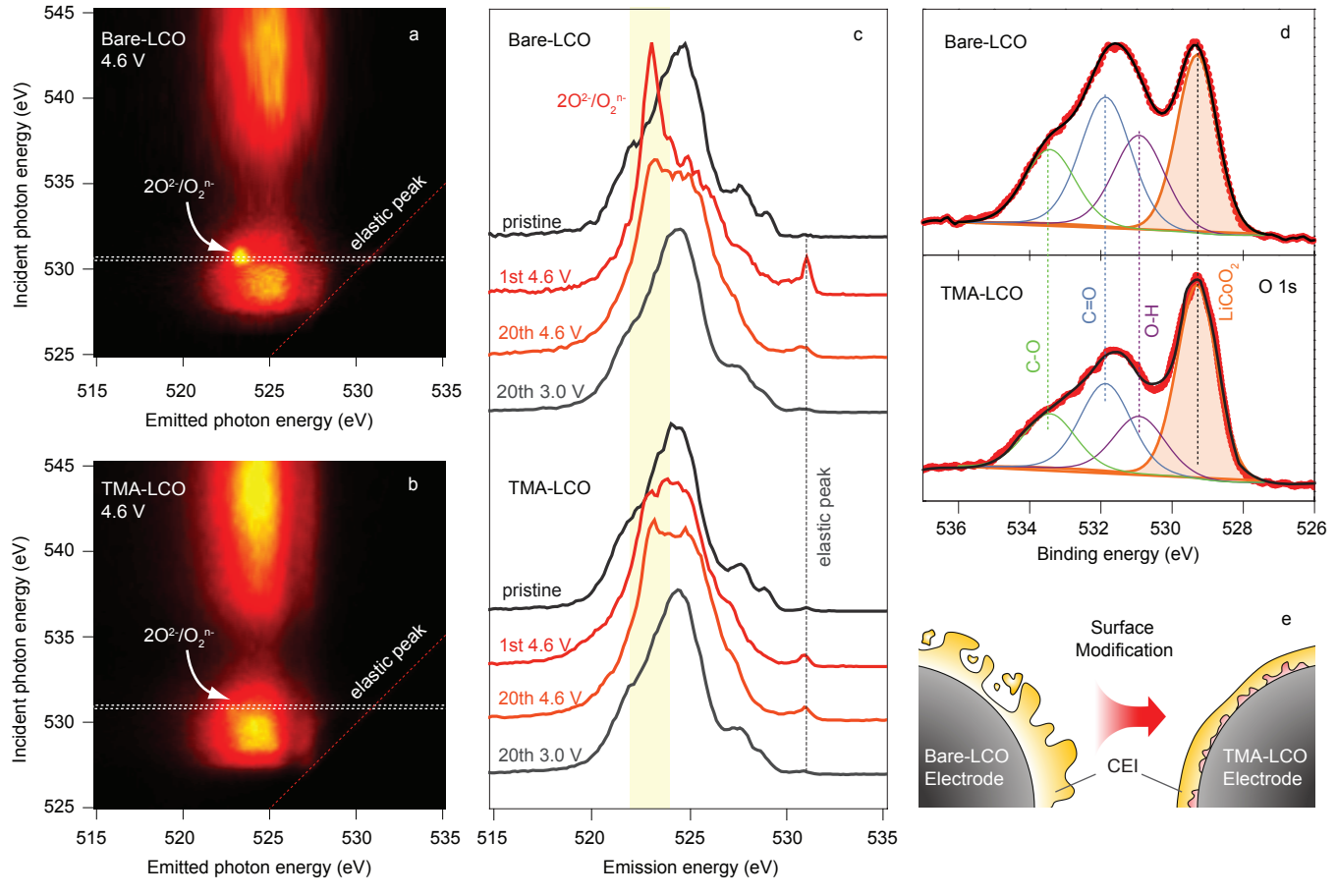
Bare-LCO
4.6 V
a
$2O^{2-}/O_2^{n-}$
elastic peak
Incident photon energy (eV)
Emitted photon energy (eV)
TMA-LCO
4.6 V
b
Bare-LCO
c
pristine
1st 4.6 V
20th 4.6 V
20th 3.0 V
TMA-LCO
elastic peak
Emission energy (eV)
Bare-LCO
d
TMA-LCO
O 1s
C-O
C=O
O-H
$LiCoO_2$
Binding energy (eV)
e
Surface Modification
Bare-LCO Electrode
CEI
TMA-LCO Electrode

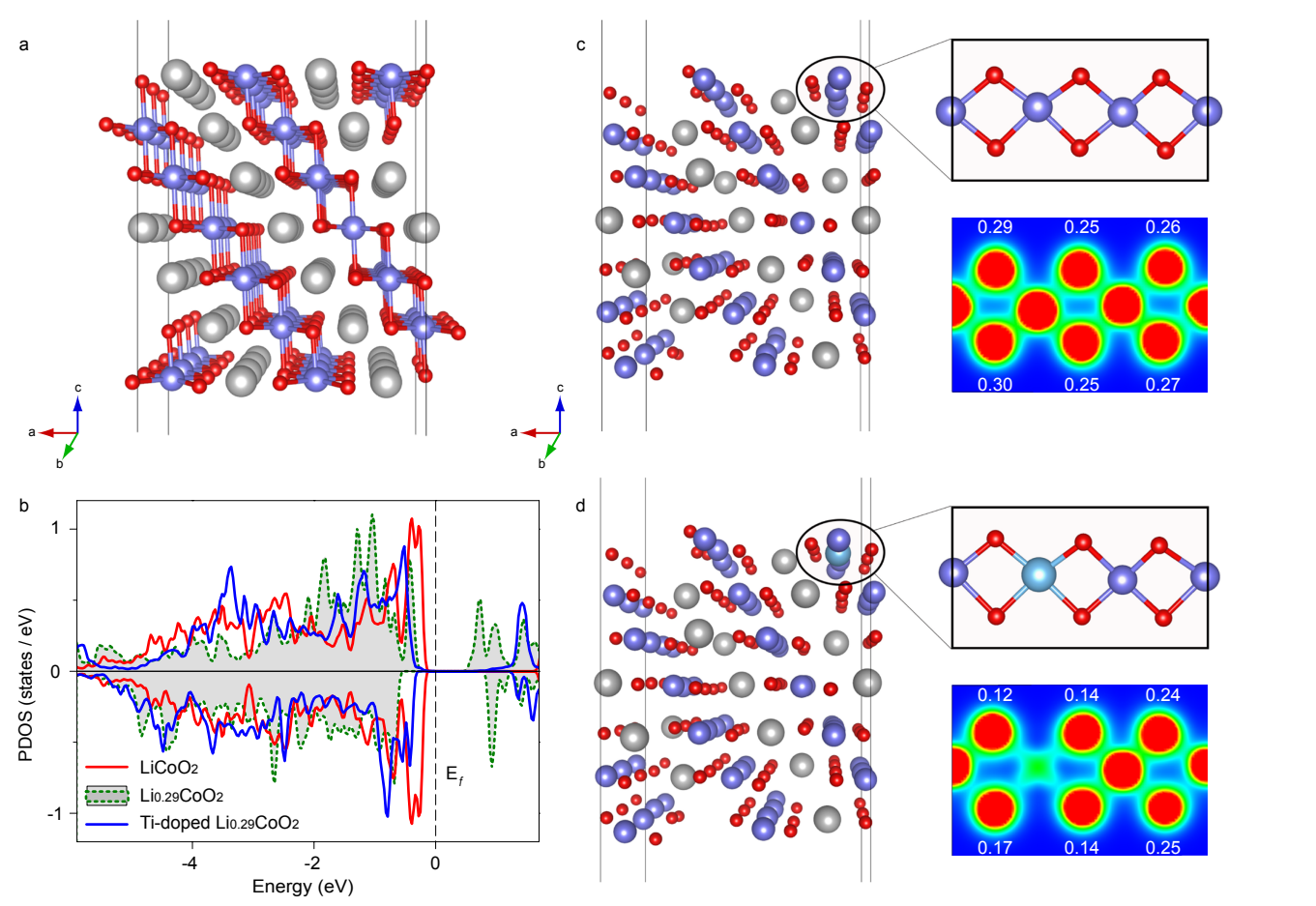
a
c
a
b
c
a
b
0.29
0.25
0.26
0.30
0.25
0.27
b
PDOS (states / eV)
1
0
-1
-4
-2
0
Energy (eV)
LiCoO2
Li0.29CoO2
Ti-doped Li0.29CoO2
Ef
d
0.12
0.14
0.24
0.17
0.14
0.25